

# We are IntechOpen, the world's leading publisher of Open Access books Built by scientists, for scientists

6,900

Open access books available

185,000

International authors and editors

200M

Downloads

Our authors are among the

154

Countries delivered to

TOP 1%

most cited scientists

12.2%

Contributors from top 500 universities



WEB OF SCIENCE™

Selection of our books indexed in the Book Citation Index  
in Web of Science™ Core Collection (BKCI)

Interested in publishing with us?  
Contact [book.department@intechopen.com](mailto:book.department@intechopen.com)

Numbers displayed above are based on latest data collected.  
For more information visit [www.intechopen.com](http://www.intechopen.com)



# Modeling & Simulation of Hysteresis Current Controlled Inverters Using MATLAB

Ahmad Albanna  
Mississippi State University  
General Motors Corporation  
United States of America

## 1. Introduction

Hysteresis inverters are used in many low and medium voltage utility applications when the inverter line current is required to track a sinusoidal reference within a specified error margin. Line harmonic generation from those inverters depends principally on the particular switching pattern applied to the valves. The switching pattern of hysteresis inverters is produced through line current feedback and it is not pre-determined unlike the case, for instance, of Sinusoidal Pulse-Width Modulation (SPWM) where the inverter switching function is independent of the instantaneous line current and the inverter harmonics can be obtained from the switching function harmonics.

This chapter derives closed-form analytical approximations of the harmonic output of single-phase half-bridge inverter employing fixed or variable band hysteresis current control. The chapter is organized as follows: the harmonic output of the fixed-band hysteresis current control is derived in Section 2, followed by similar derivations of the harmonic output of the variable-band hysteresis controller in Section 3. The developed models are validated in Section 4 through performing different simulations studies and comparing results obtained from the models to those computed from MATLAB/Simulink. The chapter is summarized and concluded in section 5.

## 2. Fixed-band hysteresis control

### 2.1 System description

Fig.1 shows a single-phase neutral-point inverter. For simplicity, we assume that the dc voltage supplied by the DG source is divided into two constant and balanced dc sources, as in the figure, each of value  $V_c$ . The  $RL$  element on the ac side represents the combined line and transformer inductance and losses. The ac source  $v_{sa}$  represents the system voltage seen at the inverter terminals. The inverter line current  $i_a$ , in Fig.1, tracks a sinusoidal reference  $i_a^* = \sqrt{2}I_a^* \sin(\omega_1 t + \phi)$  through the action of the relay band and the error current  $e_a(t) = i_a^* - i_a$ . In Fig.2, the fundamental frequency voltage at the inverter ac terminals when the line current equals the reference current is the reference voltage,  $v_a^* = \sqrt{2}V_a^* \sin(\omega_1 t + \theta)$ . Fig.2 compares the reference voltage to the instantaneous inverter voltage resulting from the action of the hysteresis loop.

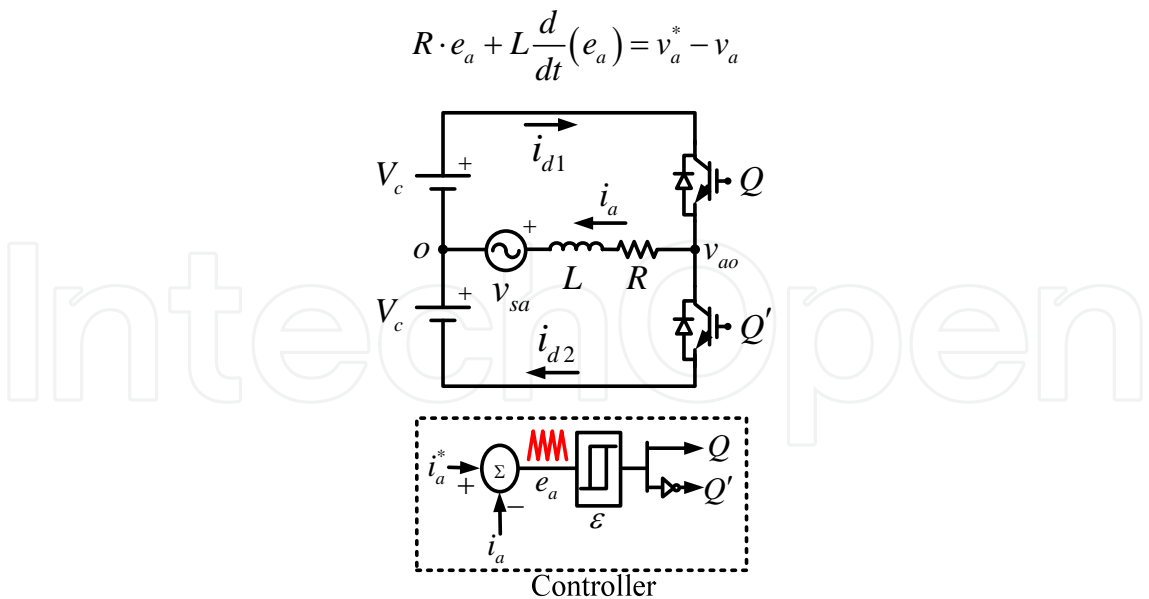


Fig. 1. Single-phase half-bridge inverter with fixed-band hysteresis control.

Referring to Fig.2, when valve  $Q$  is turned on, the inverter voltage is  $v_a = V_c > v_a^*$ ; this forces the line current  $i_a$  to slope upward until the lower limit of the relay band is reached at  $e_a(t) = -\varepsilon$ . At that moment, the relay switches on  $Q'$  and the inverter voltage becomes  $v_a = -V_c < v_a^*$ , forcing the line current to reverse downward until the upper limit of the relay band is reached at  $e_a(t) = \varepsilon$ .

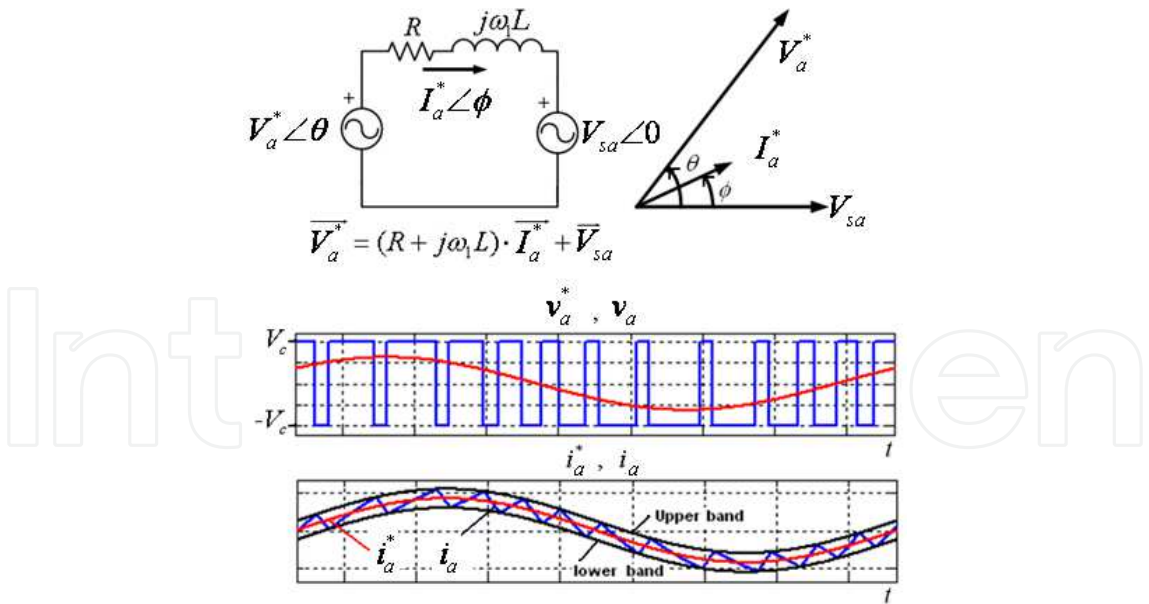


Fig. 2. Reference voltage calculation and the instantaneous outputs.

The bang-bang action delivered by the hysteresis-controlled inverter, therefore, drives the instantaneous line current to track the reference within the relay band  $(-\varepsilon, \varepsilon)$ . With reference to Fig.3 and Fig.4, the action of the hysteresis inverter described above produces an error current waveform  $e_a(t)$  close to a triangular pulse-train with modulating duty cycle and frequency.

## 2.2 Error current mathematical description

The approach described in this section closely approximates the error current produced by the fixed-band hysteresis action, by a frequency-modulated triangular signal whose time-varying characteristics are computed from the system and controller parameters. Subsequently, the harmonic spectrum of the error current is derived by calculating the Fourier transform of the complex envelope of frequency modulated signal.

Results in the literature derived the instantaneous frequency of the triangular error current  $f_{ia}(t)$  in terms of the system parameters ( $R=0$ ). Using these results and referring to Fig.3 (Albanna & Hatziadoniu, 2009, 2010):

$$t_1 = \frac{2\varepsilon L}{V_c [1 + M \sin(\omega_1 t + \theta)]}, \quad t_2 = \frac{2\varepsilon L}{V_c [1 - M \sin(\omega_1 t + \theta)]}, \quad (1)$$

and therefore:

$$f_{ia}(t) = \frac{1}{T} = f_c + \frac{V_c M^2}{8\varepsilon L} \cdot \cos(2\omega_1 t + 2\theta) \quad (2)$$

where the average switching (carrier) frequency  $f_c$  is given by

$$f_c = \frac{V_c}{4\varepsilon L} \cdot \left[ 1 - \frac{M^2}{2} \right], \quad (3)$$

and  $M$  is the amplitude modulation index of the inverter expressed in terms of the peak reference voltage and the dc voltage as:

$$M = \frac{\sqrt{2} V_a^*}{V_c}. \quad (4)$$

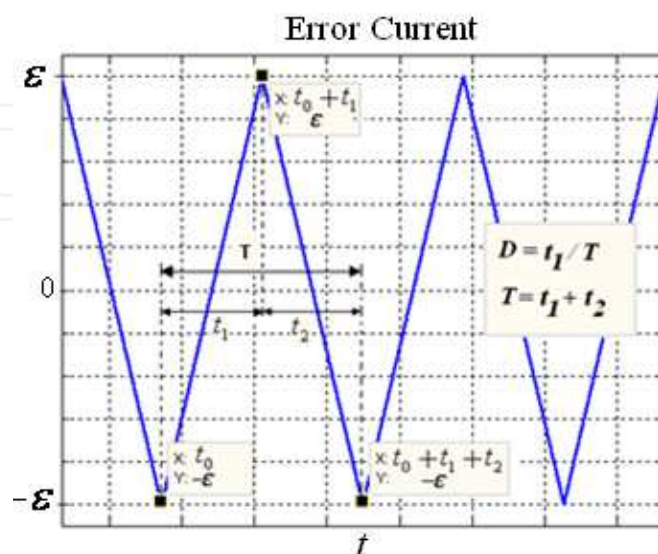


Fig. 3. Detail of  $e_a(t)$ .

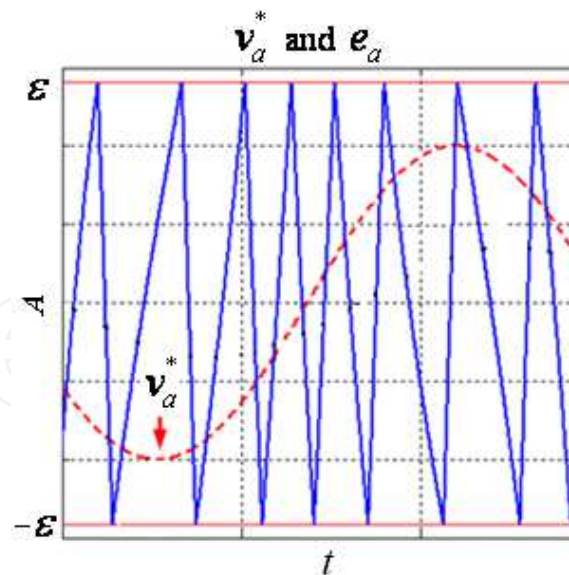


Fig. 4. Effect of  $v_a^*$  on the error current duty cycle.

Examining (2), the instantaneous frequency  $f_{ia}(t)$  of the error current  $e_a(t)$  consists of the carrier frequency  $f_c$  and a modulating part that explicitly determines the bandwidth of the error current spectrum, as it will be shown later in this chapter. Notice that the modulating frequency is twice the fundamental frequency, that is,  $2f_1$ .

Now, with the help of Fig.3, we define the instantaneous duty cycle of the error current  $D(t)$  as the ratio of the rising edge time  $t_1$  to the instantaneous period  $T$ . Noting that  $D(t) = t_1 \cdot f_{ia}(t)$ , we obtain after using (1), (2) and manipulating,

$$D(t) = 0.5 - 0.5 \cdot M \cdot \sin(\omega_1 t + \theta). \quad (5)$$

Implicit into (3) is the reference voltage  $v_a^*$ . The relation between the instantaneous duty cycle and the reference voltage can be demonstrated in Fig.4: the duty cycle reaches its maximum value at the minimum of  $v_a^*$ ; it becomes 0.5 (symmetric form) at the zero of  $v_a^*$ ; and it reaches its minimum value (tilt in the opposite direction) at the crest of  $v_a^*$ . Next, we will express  $e_a(t)$  by the Fourier series of a triangular pulse-train having an instantaneous duty cycle  $D(t)$  and an instantaneous frequency  $f_{ia}(t)$ :

$$e_a(t) = \sum_{n=1}^{\infty} \frac{-2\varepsilon}{\pi^2} \cdot \frac{(-1)^n}{n^2} \cdot \frac{\sin[n\pi(1-D(t))]}{D(t)[1-D(t)]} \cdot \sin\left(2\pi n \int_0^t f_{ia}(\tau) d\tau\right). \quad (6)$$

As the Fourier series of the triangular signal converges rapidly, the error current spectrum is approximated using the first term of the series in (6). Therefore truncating (6) to  $n=1$  and using (2) yields

$$e_a(t) \approx \frac{2\varepsilon}{\pi^2} \cdot \frac{\sin[\pi D(t)]}{D(t)[1-D(t)]} \cdot \sin(\omega_c t + \beta \sin(2\omega_1 t + 2\theta) - \varphi), \quad (7)$$

where  $\varphi = \beta \sin(2\theta)$ . The frequency modulation index

$$\beta = \frac{V_c M^2}{8\varepsilon L} \cdot \frac{1}{2f_1} \quad (8)$$

determines the frequency bandwidth

$$BW = 4(\beta + 1)f_1 \quad (9)$$

that contains 98% of the spectral energy of the modulated sinusoid in (7). To simplify (7) further, we use the following convenient approximation (see Appendix-A for the derivation): Given that,  $0 \leq D(t) \leq 1$ , then

$$\frac{\sin[\pi D(t)]}{D(t)[1-D(t)]} \approx (4-\pi) \cdot \sin[\pi D(t)] + \pi. \quad (10)$$

Therefore (7) becomes,

$$e_a(t) \approx \frac{2\varepsilon}{\pi^2} \cdot [\pi + (4-\pi)\sin(\pi D(t))] \cdot \sin(\omega_c t + \beta \sin(2\omega_1 t + 2\theta) - \varphi). \quad (11)$$

Substituting  $D(t)$  from (5) into (11) and manipulating, we obtain

$$e_a(t) \approx \frac{2\varepsilon}{\pi^2} \cdot \left( \pi + (4-\pi) \cos\left(\frac{\pi M}{2} \sin(\omega_1 t + \theta)\right) \right) \cdot \sin(\omega_c t + \beta \sin(2\omega_1 t + 2\theta) - \varphi) \quad (12)$$

Next, the cosine term in (12) is simplified by using the infinite product identity and truncating to the first term. That is,

$$\cos(x) = \prod_{n=1}^{\infty} \left( 1 - \frac{x^2}{\pi^2(n-0.5)^2} \right) \approx 1 - \frac{4x^2}{\pi^2}, \quad (13)$$

Substituting (13) into (12) and manipulating, the error current approximation becomes:

$$e_a(t) \approx \underbrace{[(8-k) + k \cos(2\omega_1 t + 2\theta)]}_{e_1(t)} \cdot \underbrace{\left[ \frac{\varepsilon}{\pi^2} \cdot \sin(\omega_c t + \beta \sin(2\omega_1 t + 2\theta) - \varphi) \right]}_{e_2(t)}, \quad (14)$$

where  $k = (4-\pi)M^2$ . The harmonic spectrum  $E_a(f)$  of the error current is the convolution of the spectra of the product terms  $e_1(t)$  and  $e_2(t)$  in (14). Therefore,

$$E_a(f) = \left[ (8-k)\delta(f) + \frac{k}{2}e^{j2\theta}\delta(f-2f_1) + \frac{k}{2}e^{-j2\theta}\delta(f+2f_1) \right] \otimes E_2(f), \quad (15)$$

where  $\otimes$  denotes convolution. In order to calculate  $E_2(f)$ , we rewrite  $e_2(t)$  as

$$e_2(t) = \frac{\varepsilon}{j2\pi^2} \left( e^{j\omega_c t} \cdot e^{-j\varphi} \cdot e^{j\beta \sin(2\omega_1 t + 2\theta)} - e^{-j\omega_c t} \cdot e^{j\varphi} \cdot e^{-j\beta \sin(2\omega_1 t + 2\theta)} \right). \quad (16)$$

The positive frequency half of the spectrum  $E_2(f)$  is therefore given by

$$E_2(f) = \frac{\varepsilon}{j2\pi^2} \sum_{n=-\infty}^{\infty} J_n(\beta) \cdot e^{j(2n\theta-\varphi)} \cdot \delta_{(f_c+2nf_1)}, \quad (17)$$

where  $\delta_x = \delta(f-x)$  is the Dirac function, and  $J_n$  is the Bessel function of the first kind and order  $n$ . Substituting (17) into (15), and convoluting, we obtain:

$$E_a(f) = \frac{\varepsilon}{j2\pi^2} \sum_{n=-\infty}^{\infty} \left( \frac{k}{2} [J_{n-1}(\beta) + J_{n+1}(\beta)] + (8-k)J_n(\beta) \right) \cdot e^{j(2n\theta-\varphi)} \cdot \delta_{(f_c+2nf_1)}. \quad (18)$$

Using the recurrence relation of the Bessel functions,

$$J_{n+1}(\beta) + J_{n-1}(\beta) = \frac{2n}{\beta} J_n(\beta), \quad (19)$$

the positive half of the error current spectrum takes the final form:

$$E_a(f) = \sum_{n=-\infty}^{n=\infty} E_n e^{j(2n\theta-\varphi)} \cdot \delta_{(f_c-2nf_1)}, \quad (20)$$

where,

$$E_n = \frac{\varepsilon}{j2\pi^2} \left( \frac{kn}{\beta} - k + 8 \right) J_n(\beta). \quad (21)$$

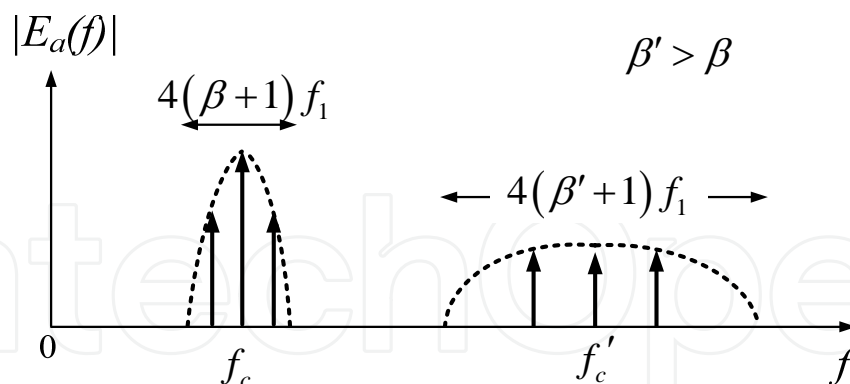


Fig. 5. Effect of changing  $\beta$  on the harmonic spectrum.

The calculation of the non-characteristic harmonic currents using (20) is easily executed numerically as it only manipulates a single array of Bessel functions. The spectral energy is distributed symmetrically around the carrier frequency  $f_c$  with spectrum bands stepped apart by  $2f_1$ . Fig.5 shows the harmonic spectrum of the error current as a function of the frequency modulation index  $\beta$ . If the operating conditions of the inverter forces  $\beta$  to increase to  $\beta'$ , then the spectral energy shifts to higher carrier frequency  $f'_c$ . Additionally, as the average spectral energy is independent of  $\beta$  and depends on the error bandwidth  $\varepsilon$ ,



the spectral energy spreads over wider range of frequencies,  $4(\beta' + 1)f_1$ , with an overall decrease in the band magnitudes to attain the average spectral energy at a constant level as shown in Fig.5. The Total Harmonic Distortion (THD) of the line current is independent of  $\beta$  and is directly proportional to the relay bandwidth  $\varepsilon$ .

### 2.3 Model approximation

The harmonic model derived in the previous section describes the exact spectral characteristics of the error current by including the duty cycle  $D(t)$  to facilitate the effect of the reference voltage  $v_a^*$  on the error current amplitude and tilting. Moreover, the consideration of  $D(t)$  in (6) predicts the amplitude of the error current precisely, which in turn, would result in accurate computation of the spectrum bands magnitudes according to (20). The model can be further simplified to serve the same functionality in without significant loss of numerical accuracy. As the instantaneous frequency of the error current, given by (2), is independent of  $D(t)$ , the spectral characteristics such as  $f_c$  and  $BW$  are also independent of  $D$  and therefore, setting  $D(t)$  to its average value 0.5 will slightly affect the magnitude of the spectrum bands according to (7). Subsequently, the error current harmonic spectrum simplifies to

$$E_a(f) = \frac{4\varepsilon}{j\pi^2} \sum_{n=-\infty}^{n=\infty} J_n(\beta) \cdot e^{j(2n\theta - \varphi)} \cdot \delta_{(f_c - 2nf_1)}, \quad (22)$$

where the carrier (average) frequency  $f_c$  is given by (3), the frequency modulation index  $\beta$  is given by (8). The 3 dB frequency bandwidth  $BW$  that contains 98% of the spectral energy is given by (9).

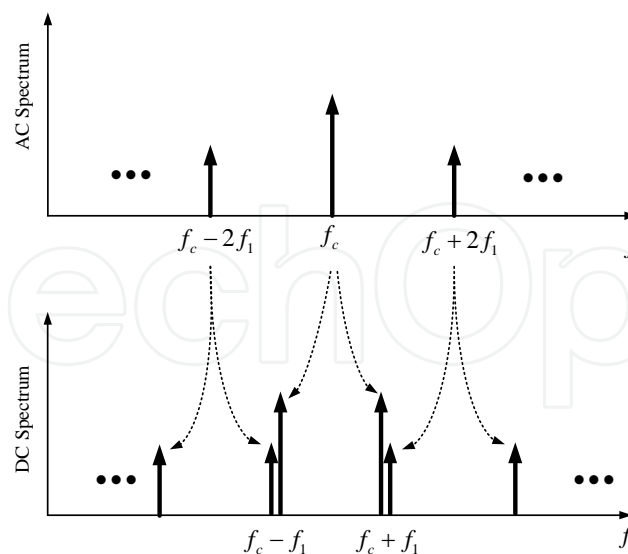


Fig. 6. AC harmonics transfer to the inverter dc side.

### 2.4 Dc current harmonics

The hysteresis switching action transfers the ac harmonic currents into the inverter dc side through the demodulation process of the inverter. As the switching function is not defined



for hysteresis inverters, the harmonic currents transfer can be modeled through balancing the instantaneous input dc and output ac power equations.

With reference to Fig.1, and assuming a small relay bandwidth (i.e.  $i_a^* \approx i_a$ ), the application of Kirchhoff Current Law (KCL) at node  $a$  gives:

$$i_{d1} = i_a^* + i_{d2}. \quad (23)$$

The power balance equation over the switching period when  $Q'$  is on is given by:

$$i_{d2} = \frac{1}{V_c} \cdot v_a(t) \cdot i_a(t). \quad (24)$$

Using the instantaneous output voltage

$$v_a = v_a^* - L \cdot \left( \frac{d}{dt} e_a \right) \quad (25)$$

in (24), the dc current  $i_{d1}$  will have the form:

$$i_{d1}(t) = \frac{v_a^* \cdot i_a^*}{V_c} + i_a^* - \frac{L}{V_c} \cdot i_a^* \cdot \left( \frac{d}{dt} e_a \right), \quad (26)$$

where  $\dot{x}$  is the derivative of  $x$  with respect to time. Using the product-to-sum trigonometric identity and simplifying yields:

$$i_{d1}(t) = \frac{\sqrt{2} M I_a^*}{2} \cos(\theta - \phi) + i_a^* - \frac{\sqrt{2} M I_a^*}{2} \cos(2\omega_1 t + \theta + \phi) - \frac{L}{V_c} \dot{e}_a \cdot i_a^*. \quad (27)$$

The positive half of the dc current spectrum is thus computed from the application of the Fourier transform and convolution properties on (27), resulting in

$$I_{d1}(f) = I_0 \cdot \delta_0 + I_1 \cdot \delta_{f_1} + I_2 \cdot \delta_{2f_1} + f \cdot I_h \cdot (E_a(f + f_1) - E_a(f - f_1)), \quad (28)$$

where  $E_a(f)$  is the error current spectrum given by (22). The average, fundamental, and harmonic components of the dc current spectrum are respectively given by

$$\begin{aligned} I_0 &= \frac{\sqrt{2}}{2} \cdot M \cdot I_a^* \cdot \cos(\theta - \phi), \\ I_1 &= \frac{\sqrt{2}}{j2} \cdot I_a^* \cdot e^{j\phi}, \quad I_2 = \frac{\sqrt{2}}{4} \cdot M \cdot I_a^* \cdot e^{j(\theta - \phi)}, \text{ and} \\ I_h &= \frac{\sqrt{2}\pi}{V_c} \cdot L \cdot I_a^*. \end{aligned} \quad (29)$$

Each spectrum band of the ac harmonic current creates two spectrum bands in the dc side due to the convolution process implicitly applied in (28). For instance, the magnitude of the ac spectrum band at  $f_c$  is first scaled by  $f_c$  according to (28) then it is shifted by  $\pm f_1$  to

create the two dc bands pinned at  $f_c \pm f_1$  as shown in Fig.6. Consequently, every two successive bands in the ac spectrum create one corresponding dc spectrum band that is located half the frequency distance between the two ac bands.

## 2.5 Harmonic generation under distorted system voltages

The harmonic performance of the hysteresis inverter in Fig.7 under distorted dc and ac system voltages is analyzed. The presence of background harmonics in the ac and dc voltages will affect the instantaneous frequency of the inverter according to (30) as

$$f'_{ia}(t) = \frac{V_c}{4\varepsilon L} \cdot \left[ 1 - \left( \frac{v_a^*}{V_c} + \frac{v_h}{V_c} - \frac{v_k}{V_c} \right)^2 \right] \quad (30)$$

where the dc distortion  $v_k$ , and the distortion of the ac system voltage,  $v_h$ , are given as:

$$\begin{aligned} v_k &= \sqrt{2}V_k \sin(k\omega_1 t + \gamma_k) \\ v_h &= \sqrt{2}V_h \sin(h\omega_1 t + \gamma_h) \end{aligned} \quad (31)$$

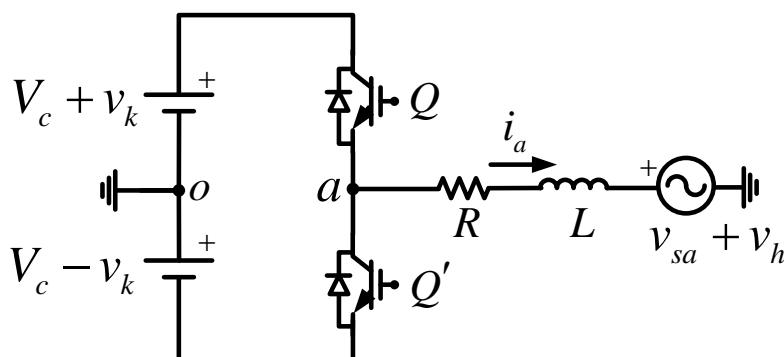


Fig. 7. Hysteresis inverter operating with distorted system voltages.

Notice that in (31),  $k$  and  $h$  need not be integers. Substituting (31) in (30) and assuming small distortion magnitudes, the instantaneous frequency of the error current  $e_a$  simplifies to:

$$f'_{ia}(t) = f_{ia}(t) - \Delta f_{ac}(t) + \Delta f_{dc}(t), \quad (32)$$

where  $f_{ia}(t)$  is given by (2) and

$$\begin{aligned} \Delta f_{ac}(t) &= \frac{V_c}{4\varepsilon L} \cdot M \cdot M_h \cdot \left[ \cos([h-1]\omega_1 t + \gamma_h - \theta) - \cos([h+1]\omega_1 t + \gamma_h + \theta) \right], \\ \Delta f_{dc}(t) &= \frac{V_c}{4\varepsilon L} \cdot M \cdot M_k \cdot \left[ \cos([k-1]\omega_1 t + \gamma_k - \theta) - \cos([k+1]\omega_1 t + \gamma_k + \theta) \right], \end{aligned} \quad (33)$$

are the frequency noise terms due to the system background distortions. The amplitude modulation indices of the ac and dc harmonic distortions are given by :

$$M_h = \frac{\sqrt{2}V_h}{V_c}, \text{ and } M_k = \frac{\sqrt{2}V_k}{V_c}. \quad (34)$$

Integrating (32), the error current  $e_a(t)$  is thus approximated by the frequency-modulated sinusoid:

$$e'_a(t) = \frac{8\varepsilon}{\pi^2} \sin[\omega_c t + \beta \sin(2\omega_1 t + 2\theta) - \varphi + \psi_{ac} + \psi_{dc}]. \quad (35)$$

In (35): the carrier frequency  $f_c$  is given by (3); the frequency modulation index  $\beta$  is given by (3);  $\varphi = \beta \sin(2\theta)$ ; and

$$\begin{aligned} \psi_{ac} &= \beta_h^+ \sin([h+1]\omega_1 t + \gamma_h + \theta) - \beta_h^- \sin([h-1]\omega_1 t + \gamma_h - \theta) + \varphi_{ac}, \\ \psi_{dc} &= \beta_k^- \sin([k-1]\omega_1 t + \gamma_k - \theta) - \beta_k^+ \sin([k+1]\omega_1 t + \gamma_k + \theta) + \varphi_{dc}. \end{aligned} \quad (36)$$

where  $\varphi_{ac} = \beta_h^- \sin(\gamma_h - \theta) - \beta_h^+ \sin(\gamma_h + \theta)$ , and  $\varphi_{dc} = \beta_k^+ \sin(\gamma_k + \theta) - \beta_k^- \sin(\gamma_k - \theta)$ . The corresponding ac and dc frequency modulation indices are given by

$$\begin{aligned} \beta_h^+ &= \frac{V_c}{4\varepsilon L} \cdot M \cdot M_h \cdot \frac{1}{(h+1) \cdot f_1} \quad ; \quad \beta_h^- = \frac{V_c}{4\varepsilon L} \cdot M \cdot M_h \cdot \frac{1}{(h-1) \cdot f_1} \quad ; \\ \beta_k^+ &= \frac{V_c}{4\varepsilon L} \cdot M \cdot M_k \cdot \frac{1}{(k+1) \cdot f_1} \quad ; \quad \beta_k^- = \frac{V_c}{4\varepsilon L} \cdot M \cdot M_k \cdot \frac{1}{(k-1) \cdot f_1}. \end{aligned} \quad (37)$$

Applying the Fourier transform and convolution properties on (35), the positive half of the frequency spectrum  $E'_a(f)$  simplifies to:

$$E'_a(f) = E_a(f) \otimes \mathfrak{I}_{ach}(f) \otimes \mathfrak{I}_{dck}(f), \quad (38)$$

Where  $E_a(f)$  is given by (22) and

$$\begin{aligned} \mathfrak{I}_{ach} &= e^{j\varphi_{ac}} \left( \sum_{n=-\infty}^{\infty} J_n(\beta_h^+) \cdot e^{jn(\gamma_h + \theta)} \cdot \delta_{(h+1)nf_1} \right) \otimes \left( \sum_{n=-\infty}^{\infty} J_n(\beta_h^-) \cdot e^{-jn(\gamma_h - \theta)} \cdot \delta_{-(h-1)nf_1} \right), \\ \mathfrak{I}_{dck} &= e^{j\varphi_{dc}} \left( \sum_{n=-\infty}^{\infty} J_n(\beta_k^+) \cdot e^{-jn(\gamma_k + \theta)} \cdot \delta_{-(k+1)nf_1} \right) \otimes \left( \sum_{n=-\infty}^{\infty} J_n(\beta_k^-) \cdot e^{jn(\gamma_k - \theta)} \cdot \delta_{(k-1)nf_1} \right), \end{aligned} \quad (39)$$

are the ac and dc modulating spectra. Generally, for any  $H$  number of ac voltage distortions and  $K$  number of dc distortions, (40) is applied first to calculate the total ac and dc modulating spectra, then (38) is used to compute the error current harmonic spectrum.

$$\begin{aligned} \mathfrak{I}_{acH}(f) &= \bigotimes_H \mathfrak{I}_{ach}, \\ \mathfrak{I}_{dcK}(f) &= \bigotimes_K \mathfrak{I}_{dck}. \end{aligned} \quad (40)$$

### 3. Variable-band hysteresis control

#### 3.1 Error current mathematical description

The harmonic line generation of the half-bridge inverter of Fig.1 under the variable-band hysteresis current control is derived. The constant switching frequency of the error current in (2), i.e.  $f_{ia}(t) = f_o$ , is achieved by limiting the amplitude of the error current to stay within the variable band [54, 55]:

$$\varepsilon_a(t) = \varepsilon_o \left[ 1 - 0.5M^2 + 0.5M^2 \cos(2\omega_1 t + 2\theta) \right], \quad (41)$$

where the maximum value of the modulating relay bandwidth is

$$\varepsilon_o = \frac{V_c}{4Lf_o}, \quad (42)$$

and  $f_o$  is the target switching frequency. Subsequently, the error current is approximated by the amplitude-modulated sinusoid of frequency  $f_o$  as:

$$e_a(t) = \frac{8}{\pi^2} \cdot \varepsilon_a(t) \cdot \sin(2\pi f_o t) \quad (43)$$

Substituting (41) in (43) and then applying the Fourier transform, the positive half of the frequency spectrum of  $E_a(f)$  is:

$$E_a(f) = \frac{4\varepsilon_o}{j\pi^2} \left[ \left( 1 - \frac{M^2}{2} \right) \delta_{f_o} + \frac{M^2}{4} \left( e^{-j2\theta} \delta_{(f_o-2f_1)} + e^{j2\theta} \delta_{(f_o+2f_1)} \right) \right]. \quad (44)$$

The error current spectrum in (44) consists of a center band at the switching frequency  $f_o$  and two side bands located at  $f_o \pm 2f_1$ . The frequency bandwidth that contains the spectral energy of (44) is simply  $4f_1$ .

#### 3.2 Dc current harmonics

The approach developed in 2.2.4 also applies to compute the dc current harmonic spectrum when the variable-band hysteresis control. The positive half of the dc current harmonic spectrum is computed by substituting (44) in (28).

#### 3.3 Harmonic generation under distorted system voltages

The presence of background harmonics in the ac and dc voltages, given in (31) will affect the instantaneous frequency of the inverter according to (30). Subsequently, to achieve the constant switching frequency  $f_o$ , the modulating error band in (41) will also contain the corresponding distortions terms as

$$\varepsilon_a(t) = \varepsilon_a^o(t) - \varepsilon_a^{ac}(t) + \varepsilon_a^{dc}(t), \quad (45)$$

where  $\varepsilon_a^o(t)$  is the error under zero background distortion given by (41), and

$$\begin{aligned}\varepsilon_a^{ac}(t) &= 2\varepsilon_o MM_h \sin(h\omega_1 t + \gamma_h) \sin(\omega_1 t + \theta), \\ \varepsilon_a^{dc}(t) &= 2\varepsilon_o MM_k \sin(k\omega_1 t + \gamma_k) \sin(\omega_1 t + \theta),\end{aligned}\quad (46)$$

where  $M_h$  and  $M_k$  define the modulation index of the ac and dc background distortion terms respectively as (34).

The new terms introduced by the background distortion appear as amplitude modulations in (45). The error current  $e'_a(t)$  is then expressed as:

$$e'_a(t) = \frac{8}{\pi^2} [\varepsilon_a^o(t) - \varepsilon_a^{ac}(t) + \varepsilon_a^{dc}(t)] \sin(2\pi f_o t). \quad (47)$$

The harmonic spectrum of the error current  $E'_a(f)$  simplifies to

$$E'_a(t) = E_a(f) - E_a^{ac}(f) + E_a^{dc}(f), \quad (48)$$

where  $E_a(f)$  is the zero-background-distortion error as in (44), and the new terms due to background distortion:

$$\begin{aligned}E_a^{ac} &= \frac{2MM_h \varepsilon_o}{j\pi^2} \cdot \left[ e^{j(\gamma_h - \theta)} \cdot \delta_{f_o + (h-1)f_1} + e^{-j(\gamma_h - \theta)} \cdot \delta_{f_o - (h-1)f_1} \right. \\ &\quad \left. - e^{j(\gamma_h + \theta)} \delta_{f_o + (h+1)f_1} - e^{-j(\gamma_h + \theta)} \cdot \delta_{f_o - (h+1)f_1} \right], \\ E_a^{dc} &= \frac{2MM_k \varepsilon_o}{j\pi^2} \cdot \left[ e^{j(\gamma_k - \theta)} \cdot \delta_{f_o + (k-1)f_1} + e^{-j(\gamma_k - \theta)} \cdot \delta_{f_o - (k-1)f_1} \right. \\ &\quad \left. - e^{j(\gamma_k + \theta)} \cdot \delta_{f_o + (k+1)f_1} - e^{-j(\gamma_k + \theta)} \cdot \delta_{f_o - (k+1)f_1} \right].\end{aligned}\quad (49)$$

Examining (49), the presence of the harmonic distortions in the system tends to scatter the spectrum over lower frequencies, more specifically, to  $f_o - (h+1)f_1$ , for  $h > k$  or to  $f_o - (k+1)f_1$  for  $k > h$ .

## 4. Simulation

The harmonic performance of the half-bridge inverter under the fixed- and variable-band hysteresis control is analyzed. Results computed from the developed models are compared to those obtained from time-domain simulations using MATLAB/Simulink. Multiple simulation studies are conducted to study the harmonic response of the inverter under line and control parameter variations. The grid-connected inverter of Fig.1 is simulated in Simulink using:  $V_c = 400\text{ V}$ ,  $V_{sa} = 120\text{ V}_{rms}$ ,  $f_1 = 60\text{ Hz}$ ,  $R = 1.88\ \Omega$ , and  $L = 20\text{ mH}$ . In order to limit the THD of the line current to 10%, the line current tracks the sinusoidal reference  $i_a^* = \sqrt{2} \cdot 15 \cdot \sin(\omega_1 t)\text{ A}$  within the maximum relay bandwidth of  $\varepsilon = \varepsilon_o = 2.82\text{ A}$ .

### 4.1 Fixed-band hysteresis current control

The ac outputs of the half-bridge inverter under the fixed-band hysteresis current control are shown in Fig.8. the fundamental component  $v_a^*$  of the bipolar output voltage  $v_a$  has a

peak value of 263.7 V. the inverter line current  $i_a$  tracks the sinusoidal reference within an absolute error margin  $\varepsilon$  . The error current resulting from the fixed-band hysteresis action resembles a frequency-modulate triangular signal of constant amplitude. The implicit relation between the error current duty cycle and the reference voltage  $v_a^*$  is clearly seen in Fig.8. The symmetric duty cycle, i.e.  $D=0.5$  , happens whenever the reference voltage approaches a zero crossing.

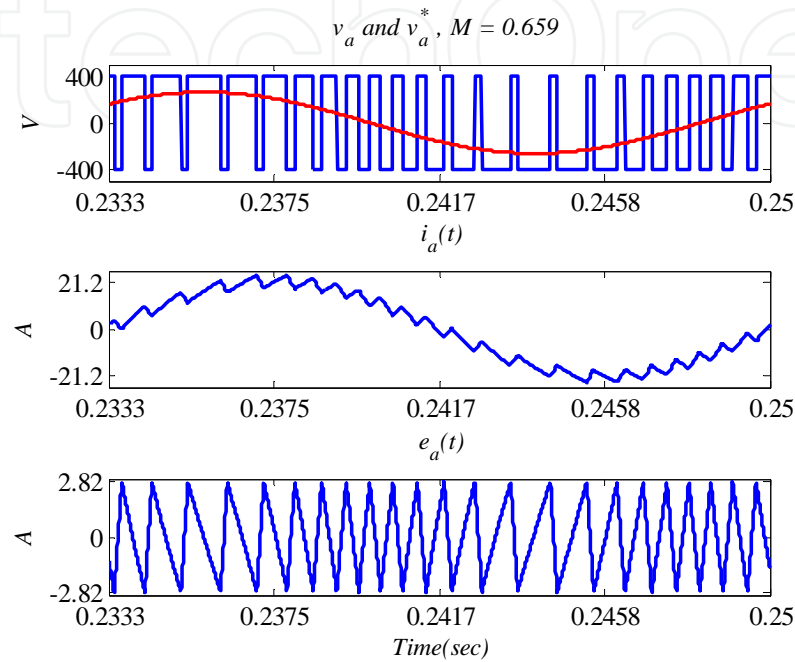


Fig. 8. Inverter ac outputs under fixed-band hysteresis control.

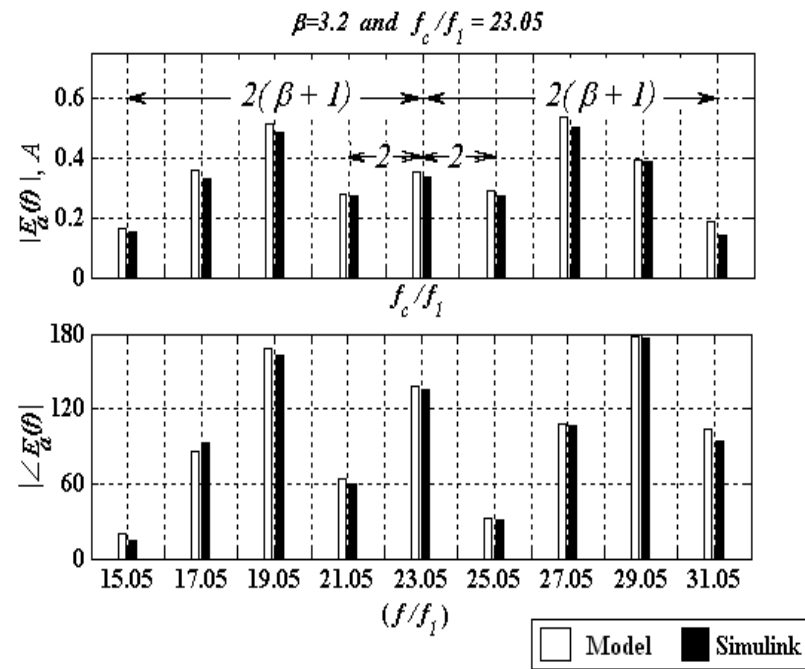


Fig. 9. Simulation results obtained from the developed model and Simulink.

The harmonic parameters of the model are computed the system and controller parameters as follows: substituting the reference voltage in (4) results in an amplitude modulation index of  $M = 0.659$ ; from (3), the carrier frequency is  $f_c = 23.05 f_1 = 1383 \text{ Hz}$ ; and from (8), the frequency modulation index is  $\beta = 3.2$ . Fig.9 compares the harmonic spectrum of the error current  $E_a(f)$  computed from (20) to that obtained from the Fourier analysis of the time-domain simulation results using Simulink. The figure shows a good agreement between the two spectra in terms of frequency order, magnitude and angle.

The spectrum bands are concentrated around the order of the carrier frequency and are stepped apart by two fundamental frequency orders  $2f_1$  as shown in Fig.9. With reference to (9) and Fig.9, it is shown that 98% of the spectrum power is laying in the bandwidth  $BW = 4(\beta + 1)f_1 \approx 16f_1$ . Therefore, the spectrum bands outside this range contribute insignificantly to the total spectrum power and thus can be truncated from the spectrum for easier numerical applications.

To study the effect of line parameter variations on the harmonic performance of the inverter, the DG source voltage is decreased to have the dc voltage  $V_c = 350 \text{ V}$ , then the harmonic spectrum is recomputed using the model and compared to the results obtained from Simulink. Decreasing  $V_c$  will increase  $M$  and  $\beta$  according to (4) and (8) respectively, but will decrease  $f_c$  according to (3).

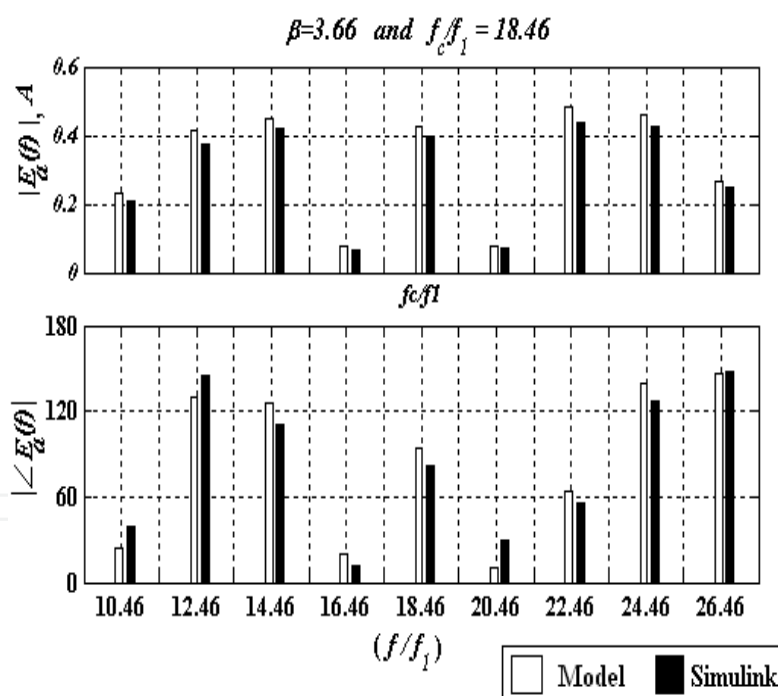


Fig. 10.  $E_a(f)$  when  $V_c$  is decreased to 350V.

With reference to the results shown in Fig.10, the harmonic spectrum  $E_a(f)$  will shift to the lower frequency order of, approximately, 18, and will span a wider range, as  $\beta$  is greater. The frequency bandwidth has slightly increased to  $18f_1$  from the previous value of  $16f_1$  due to the slight increase in  $\beta = 3.2$  to  $\beta = 3.66$ .

The total spectral energy of the error current depends on the relay bandwidth  $\varepsilon$  and it is independent of  $\beta$ . As  $\beta$  increases the spectrum energy redistributes such that the bands



closer to  $f_c$  decrease in magnitude and those that are farther from  $f_c$  increase as shown in Fig.10. The Total Harmonic Distortion (THD) of the line current thus will not be affected by changing  $V_c$ .

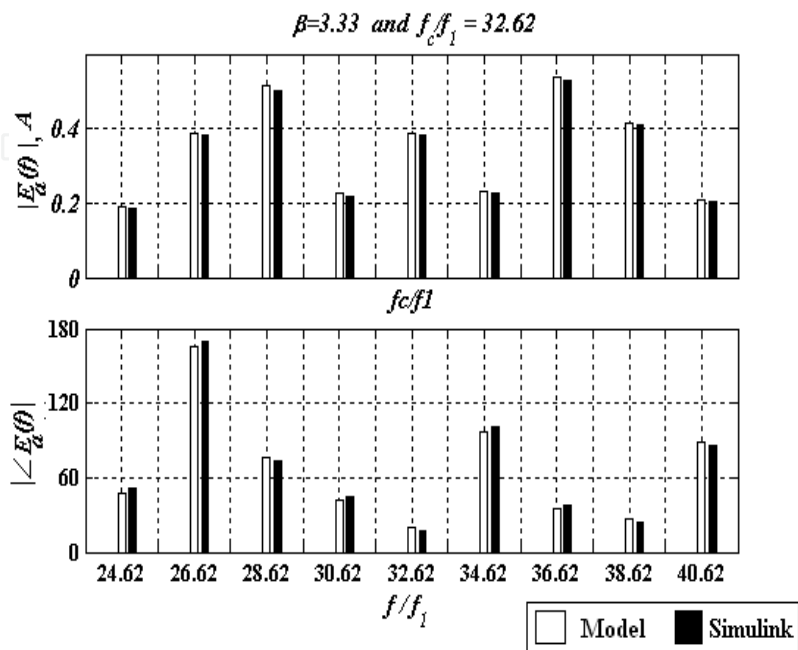


Fig. 11.  $|E_a(f)|$  when the system inductance is decreased by 25%.

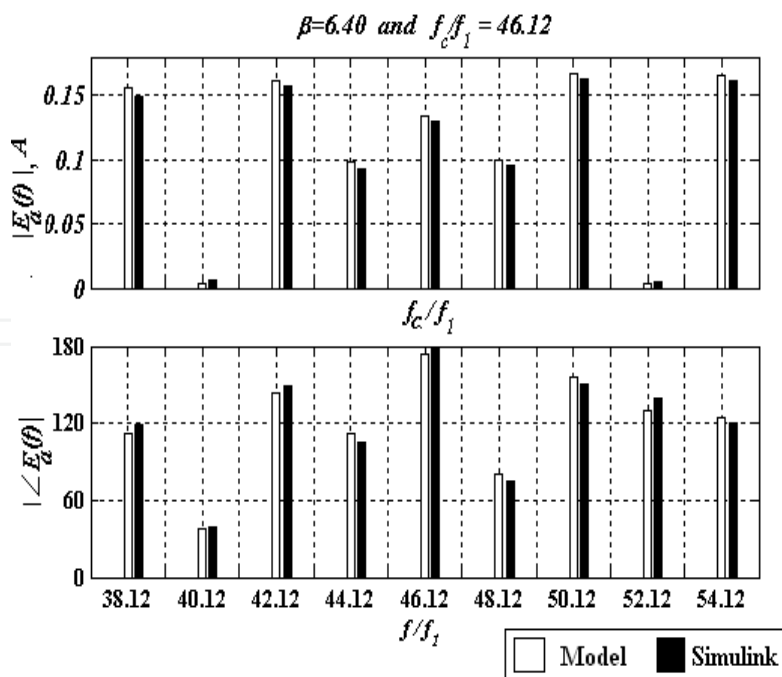


Fig. 12. Results from reducing  $\varepsilon$  by 50%.

Next, the system and control parameters are set to their original values and the inductance is decreased by 25% to  $L = 15\text{ mH}$ . The results are shown in Fig.11. Lower inductance results

in higher switching frequency according to (3) and higher  $\beta$  according to (8). The harmonic spectrum  $E_a(f)$  shifts to higher frequencies as  $f_c$  is increasing, and the spectrum spans a wider range as  $\beta$  is increasing. The amplitude modulation index  $M$  and  $D$  are affected by the system inductance variation since the inverter reference voltage  $v_a^*$  depends on system inductance  $L$ .

The width of the relay band is reduced by half while maintaining the rest of the parameters at their base values. As (4) indicates,  $M$  is independent of  $\varepsilon$  and thus it remains unchanged from its value of 0.659. Referring to Fig.12, as the error band is reduced by half, the carrier frequency doubles and the harmonic spectrum  $E_a(f)$  will be concentrated around, approximately, the order of 46. The frequency modulation index  $\beta$  doubles and thus the spectrum spreads over a wider frequency range overall decreasing in magnitude, as seen in Fig.12. Under these conditions, the THD of the line current will decrease to approximately 5% as the spectral energy of the spectrum is proportional to the relay bandwidth  $\varepsilon$ .

To study the harmonic performance of the inverter under distorted system voltages, the system and control parameters are set to the original values and the 11<sup>th</sup> order voltage oscillator  $v_{11}(t) = 15 \cdot \sin(11 \cdot \omega_1 t)$  V is included in the source voltage  $v_s$  to simulate a distorted ac network voltage. The simulation is run for 30 fundamental periods to ensure solution transients are vanishing, and the last fundamental period of the inverter ac outputs are shown in Fig.13.

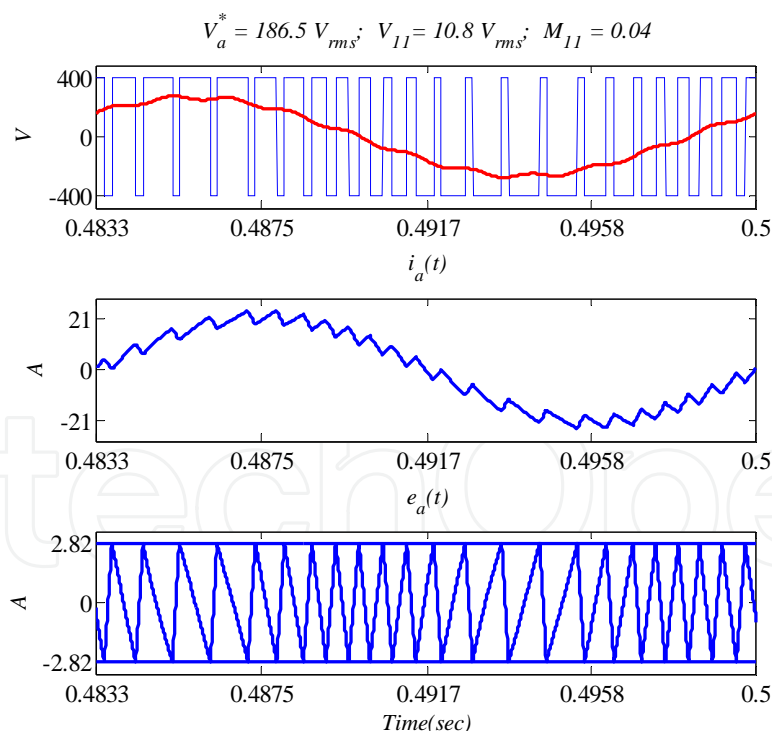


Fig. 13. Effect of injecting the 11<sup>th</sup> ac harmonic voltage on the inverter ac outputs.

Comparing Fig.8 and Fig.13, the reference voltage is distorted due to the presence of the 11<sup>th</sup> voltage oscillator in the source. The output voltage of the inverter is still bipolar, i.e.  $v_a = \pm 400$  V. Fig. 14 compares the instantaneous frequency of the error current under sinusoidal ac voltage  $f_{ia}$  to that under the distorted ac system voltage  $f'_{ia}$ .

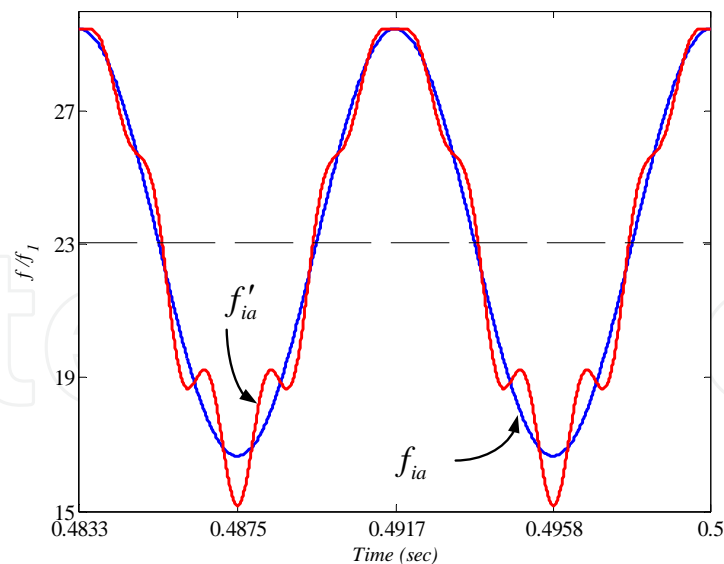


Fig. 14. Instantaneous frequency of  $e_a(t)$  when  $v_s$  is distorted.

According to (32), the carrier frequency  $f_c = 23.05f_1$  is constant and independent of the distortion terms. The amplitude modulation index  $M_{11} = 0.038$  is computed from (34), subsequently, the harmonic parameters  $\beta_{11}^+ = 0.062$  and  $\beta_{11}^- = 0.074$  are computed from (37).

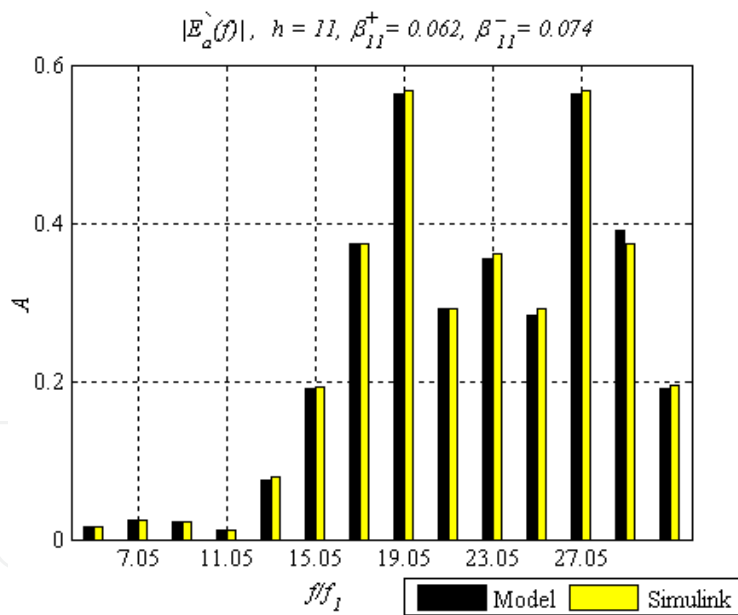


Fig. 15. Error spectrum when  $v_{sa}$  contains the 11<sup>th</sup> oscillator voltage.

Fig.15 compares the harmonic spectrum  $E'_a(f)$  obtained from (38) to that computed from the Fourier analysis of Simulink outputs with very good agreement in terms of frequency order and magnitude. The spectral energy is centered on the carrier frequency  $f_c = 23.05f_1$  with spectrum bands are stepped apart by  $2f_1$ . The frequency bandwidth increases due to the distortion terms, and as Fig.15 shows, the spectrum bands leak to as low of a frequency order as 5. Notice that the THD of the line current did not change as the controller bandwidth did not change.

Similar analysis is performed to study the harmonic performance of the inverter when the dc voltage contains the distortion  $v_8(t) = 28.2 \cdot \sin(8\omega_1 t) \text{ V}$ . The inverter instantaneous outputs obtained from Simulink are shown in Fig.16. Notice that the voltage  $v_a$  is still bipolar but distorted.

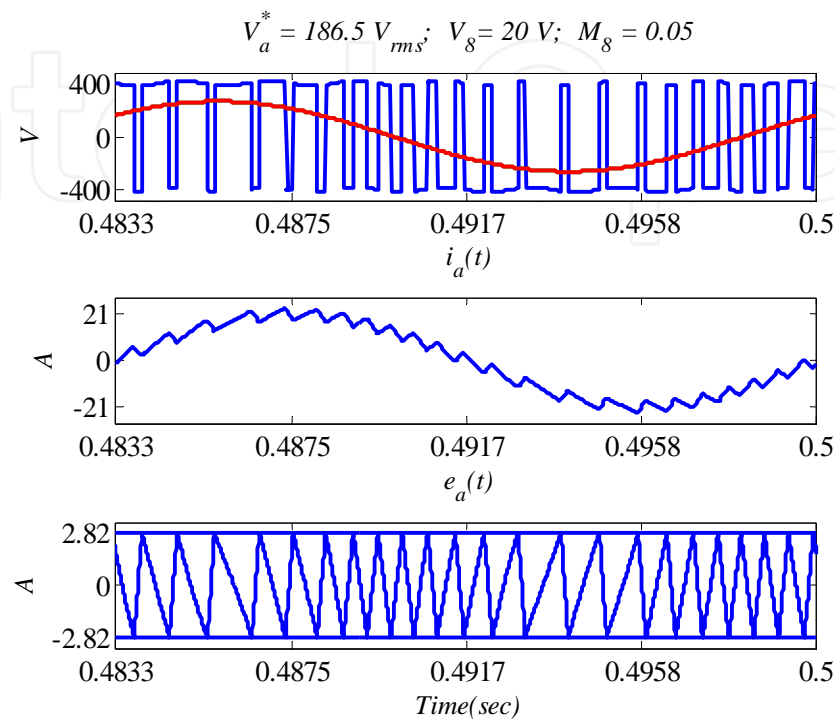


Fig. 16. Effect of injecting the 8<sup>th</sup> dc harmonic voltage on the inverter ac outputs.

The dc distortions impose additional noise component on the instantaneous frequency, see Fig.17, and subsequently, according to (38) the harmonic spectrum is drifting to lower order harmonics as shown in Fig.18.

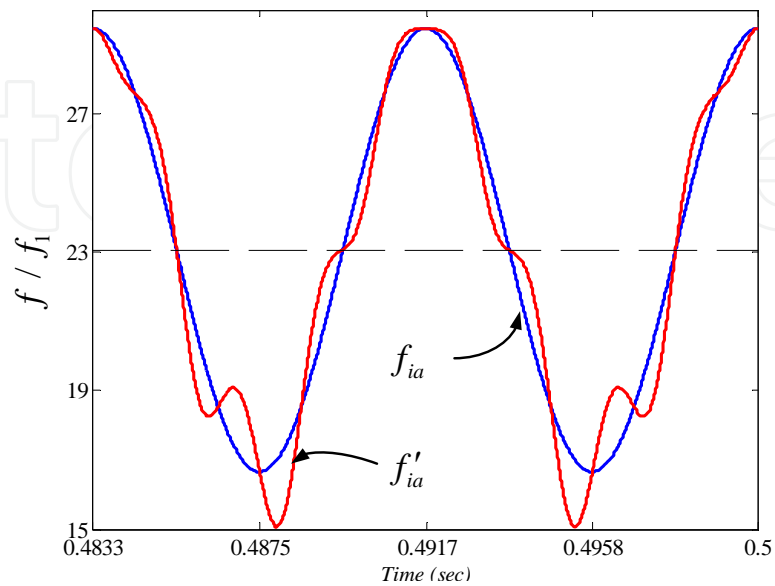


Fig. 17. Frequency of  $e_a(t)$  when the input dc is distorted.

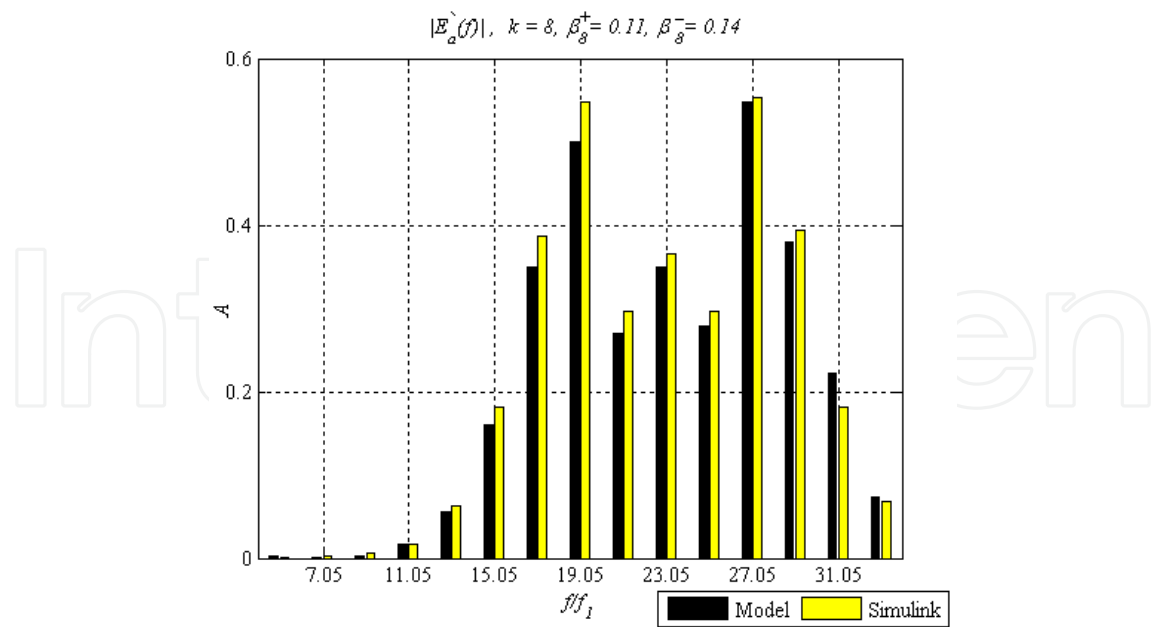


Fig. 18. Error spectrum when the 8<sup>th</sup> dc background distortion exists.

4.2 Variable-band hysteresis control

The harmonic performance of the same half-bridge inverter used in section 2.4.1 is analyzed when the variable-band hysteresis current control is employed. Similar harmonic studies to those in the previous section are performed to compute the spectral characteristics of the inverter harmonic outputs using the developed models in section 2.3 and compare them with results obtained from time-domain simulations using Simulink.

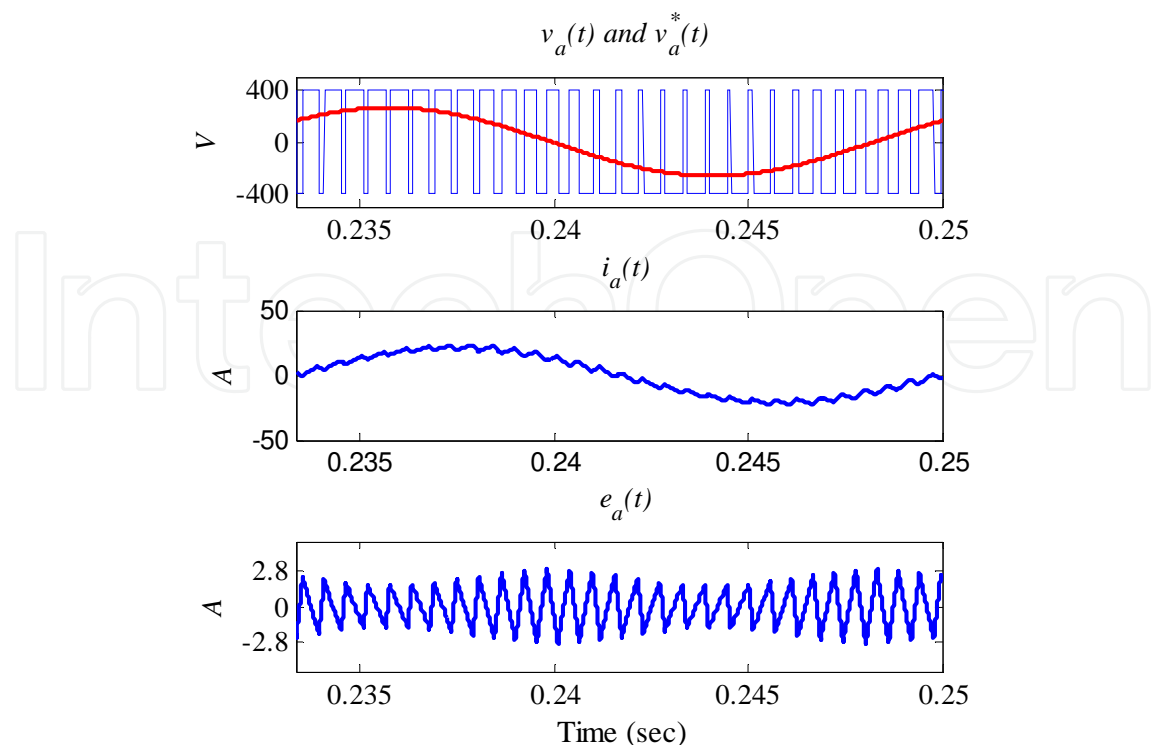


Fig. 19. Instantaneous outputs of the variable-band hysteresis control.

The instantaneous line outputs of the single-phase inverter operating under variable hysteresis control are shown in Fig.19. With the maximum relay band  $\varepsilon_o$  is set to 2.82, the error current  $e_a(t)$  resulting from the variable-band control is an amplitude-modulated triangular signal of carrier frequency  $f_o$ . Regardless of the adopted switching pattern, the reference voltage is  $v_a^* = 263.7 \cdot \sin(\omega_1 t + 37^\circ)$  V and hence,  $M = 0.659$ . From (42), the average frequency is  $f_o = 29.4 f_1$ . Fig.20 compares the spectrum  $E_a(f)$  computed from (44) to that computed from the harmonic analysis of time-domain simulation of the inverter using Simulink. The figure shows a good agreement between the two spectra in terms of frequency order and magnitude. The center band is located at  $f_o = 29.4 \cdot f_1$  and the side bands are stepped by  $2f_1$  as shown in Fig.20. The spectral energy of  $E_a(f)$  is distributed over the frequency range  $27.4 f_1$  to  $31.4 f_1$  (i.e.  $BW = 4 \cdot f_1$ ).

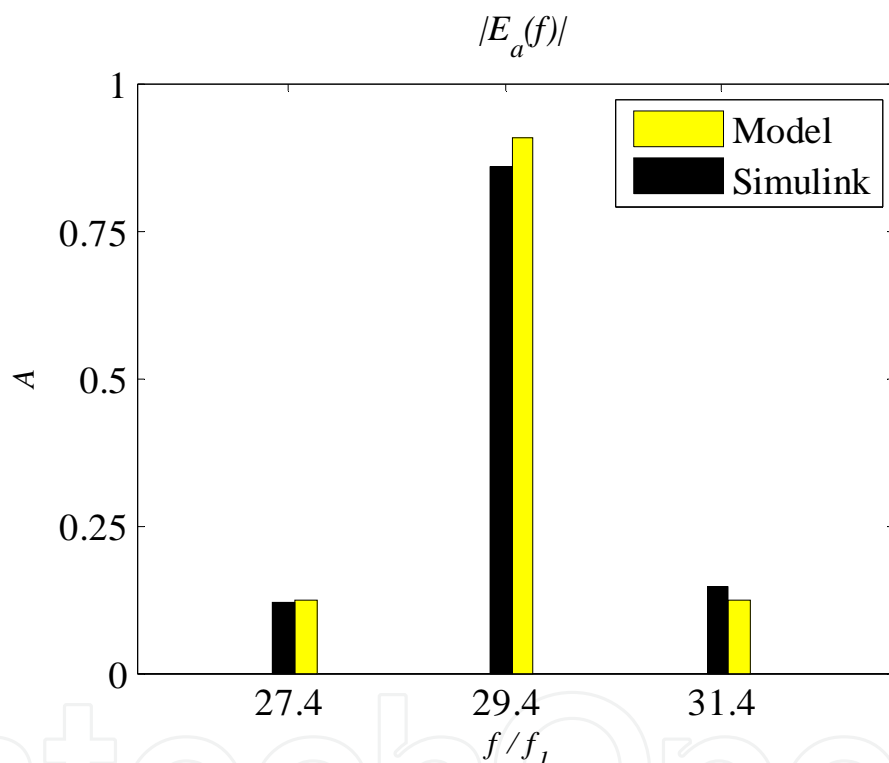


Fig. 20. Comparing model results to Simulink.

The dc voltage  $V_c$  was decreased to 350V while all other parameters remain unchanged from Study 1. Decreasing  $V_c$  will decrease  $f_o$  according to (42).

The new values are shown in Fig.21. Consequently, the spectrum  $E_a(f)$  will shift to the lower frequency order of, approximately, 25.7, while spanning over the constant bandwidth of  $4f_1$ . The spectral magnitudes of  $E_a(f)$  depend on the relay bandwidth  $\varepsilon_o$  and  $M$ ; therefore, with fixing  $\varepsilon_o$  and decreasing  $V_c$ , according to (44), the center band magnitude decreases as  $M$  is increasing. While the magnitudes of the side bands are directly proportional to  $M$ , their magnitudes will increase. This is clear from comparing the harmonic in Fig.21 to that of Fig.20. Similar to the fixed-band control, the Total Harmonic Distortion (THD) of the line current is independent of  $V_c$ .

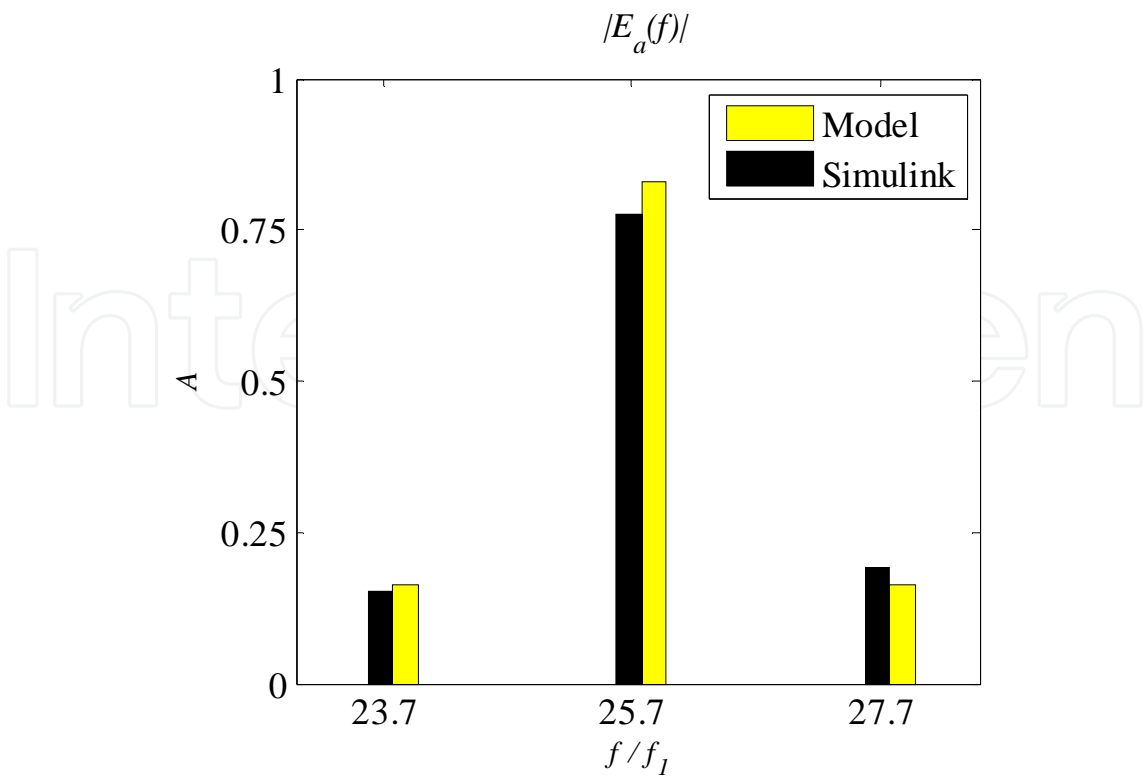


Fig. 21. Error spectra when  $V_c = 350\text{ V}$ .

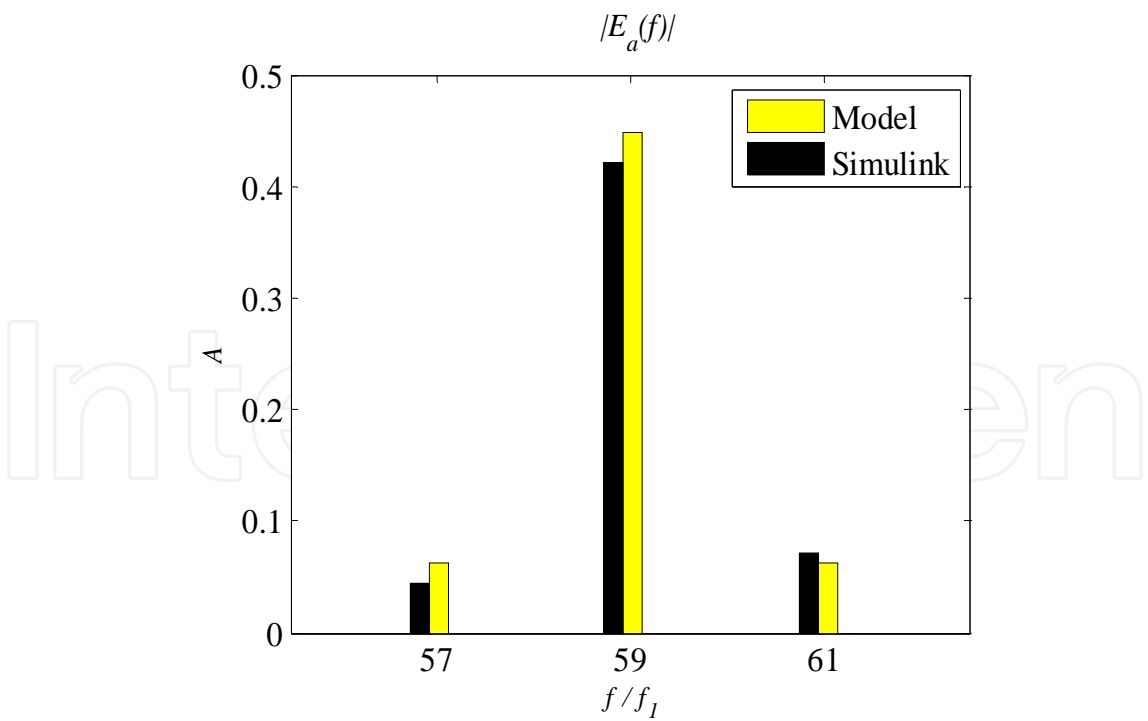


Fig. 22. Error spectra when relay bandwidth is halved.

when  $\varepsilon_o$  is halved, the carrier frequency  $f_o$  doubles and the harmonic spectrum  $E_a(f)$  will be concentrated around, approximately, the order of 59. The THD of the line current will



decrease to as low as 5% since  $\varepsilon_o$  decreases. This is demonstrated when comparing the harmonic spectra of Fig.22 and Fig.20.

The value of the inductance is decreased to  $L = 15\text{ mH}$  . The results are shown in Fig.23.

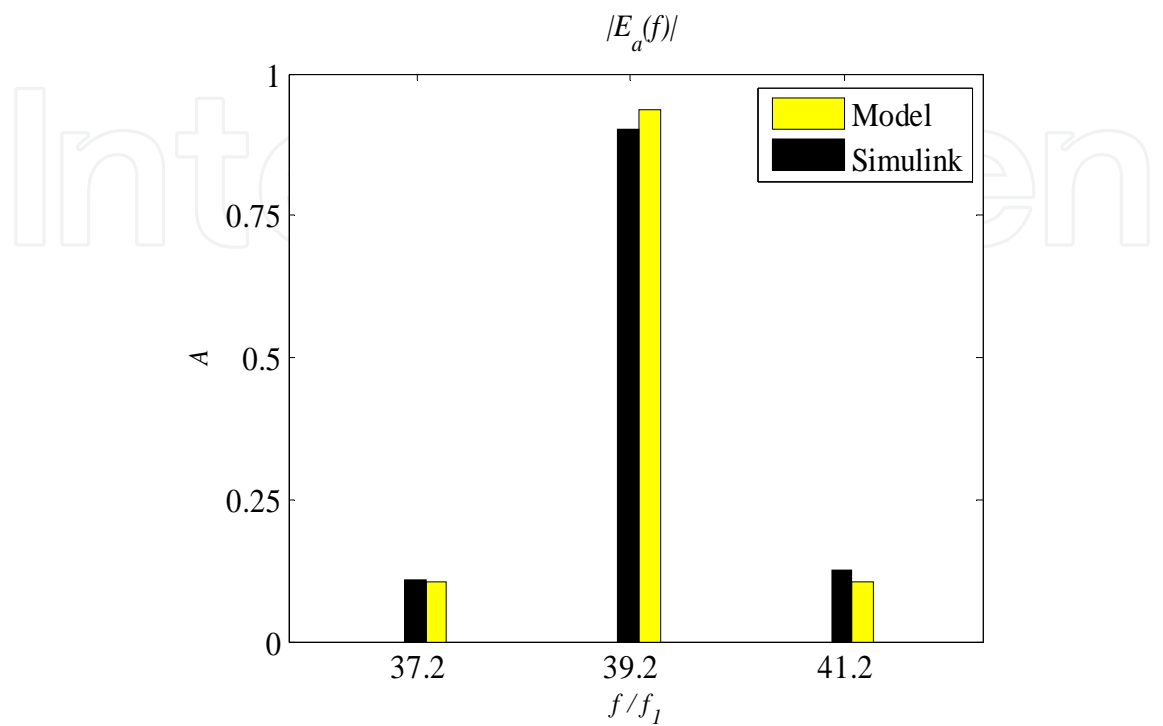


Fig. 23. Inverter harmonic response to 25% reduction in  $L$ .

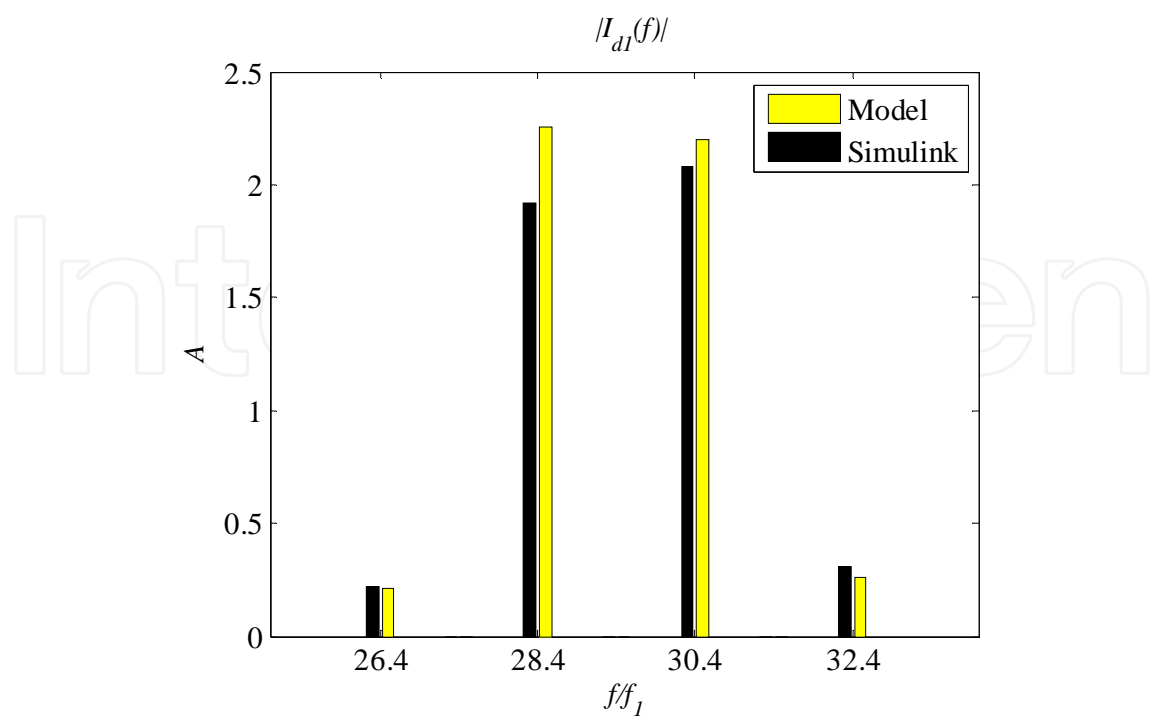


Fig. 24. DC current harmonics under variable-band control.

Lower inductance results in higher switching frequency. The harmonic spectrum  $E_a(f)$  shifts to higher frequencies as  $f_o$  is increasing to  $39.2f_1$ . As  $M$  is directly proportional to the system inductance,  $M$  decreases and therefore, the magnitude of the center band slightly increases while the side bands decrease in magnitude as shown in Fig.23. The dc current harmonics are computed from substituting (44) in (28). The resulting spectra are shown in Fig.24 with good agreement in terms of frequency orders and magnitudes.

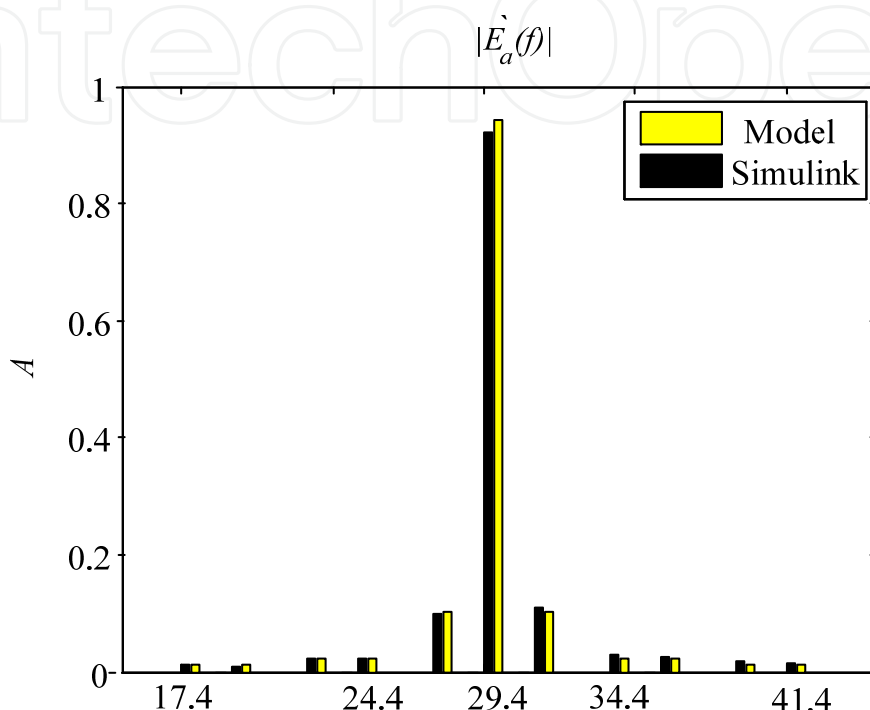


Fig. 25. Error current under distorted dc and ac system voltages.

The harmonic performance of the inverter under distorted system voltages is studied by simulating the system with the distorted 8<sup>th</sup> order dc voltage  $v_8(t) = 28.2 \cdot \sin(8\omega_1 t)$  V and the 11<sup>th</sup> order ac voltage  $v_{11}(t) = 15 \cdot \sin(11 \cdot \omega_1 t)$  V. Results obtained from model using (48) and (49) are compared to those computed from Simulink in Fig.25, the model predicts the frequency distribution of the dc current harmonics and accurately predicts their magnitudes.

#### 4.3 Comparison and discussion

The spectral characteristics of the line current under the fixed- and variable-band hysteresis control are compared in this section. For identical system configurations and controller settings, i.e.  $\varepsilon = \varepsilon_o$ , the analytical relation between  $f_c$  and  $f_o$  is stated in terms of the amplitude modulation index  $M$  as:  $f_c = (1 - 0.5M^2) \cdot f_o$ . The inverter operates at higher switching frequency when it employs the variable-band hysteresis control. In addition, from a harmonic perspective, the frequency bandwidth of  $E_a(f)$  in the variable-band control mode is constant ( $4f_1$ ) and independent of the system and controller parameters; unlike the fixed-band controller where the bandwidth  $BW$  depends implicitly on the system and controller parameters through the frequency modulation index  $\beta$ .

The THD of the line current is directly proportional to relay bandwidth. For similar controllers setting  $\varepsilon = \varepsilon_o$ , the THD is constant as the average spectral energy of the line current is constant. In fixed- and variable-band modes, the variation of system parameters shifts the spectral energy of  $E_a(f)$  to higher or lower frequency orders (depending on the carrier frequency), while simultaneously redistributing the spectral energy over the frequency bandwidth  $BW$ . The spectral energy of the error current is independent of system parameters; and hence, the THD of the line current is constant for different system settings.

## 5. Conclusion

A closed-form numerically efficient approximation for the error current harmonic spectrum of single-phase two-level inverters employing either fixed- or variable-band hysteresis current control is derived. The models are based on the amplitude and frequency modulation theorems.

The instantaneous frequency of the inverter is first derived. Then it is used to closely approximate the error current by a modulated sinusoid. The error current harmonic spectrum is basically the Fourier transform of error current complex envelop. In the case of the fixed-band control, the spectrum reduces to a series of Bessel functions of the first kind whose argument is implicitly expressed in terms of the system and controller parameters, where as in the variable-band mode, the spectrum reduces to a 3-element array.

The spectral characteristics such as the carrier frequency and frequency bandwidth are derived analytically and related to line parameters; it is a development useful in inverter-network harmonic interactions. Unlike time-domain simulators, the developed models provide fast numerical solution of the harmonic spectrum as they only involve numerical computation of single arrays. Simulation results agree closely with the developed frequency-domain models in terms of frequency order, magnitude and angle.

In addition to the single-phase two-level inverter, the proposed approximations apply also to the harmonic output of certain three-phase two-level inverters where independent phase control is applicable, such as the neutral point inverter, and the full-bridge inverter in bipolar operation.

## 6. Future directions of research

The models detailed in this chapter can be extended in a number of ways, both in terms of improving the proposed models as well as in the application of the models in other PWM applications.

The developed models neglected the dynamics of the Phase-Locked Loop (PLL) and assumed that the inverter line current tracks a pure sinusoidal reference current. Possible extensions of the models include the effect of the harmonic current propagation through the ac network and the deterioration of the terminal voltage at the interface level and its effect on the reference current generation. As the PLL synchronizes the reference current with the terminal voltage, the propagation of harmonic currents might affect the detection of the zeros-crossings of the terminal voltage resulting in generating a distorted reference current. The hysteresis controller consequently will force the line current to track a non-sinusoidal reference which, in turn, modifies the harmonic output of the inverter.

The implementation of an LC filter at the inverter ac terminals could trigger a parallel-resonance which tends to amplify the harmonic voltages and currents in the ac network

leading, in some cases, to potential harmonic instabilities. The improvement of the developed models to include the effect the filter capacitance on the harmonic performance of the inverter is an interesting improvement.

Reviews of the developed models show that hysteresis current controlled inverters can have a 'switching function' notation similar to those inherit with the Sinusoidal PWM inverters. The switching function is based on the error current characteristics which implicitly depend on the system and controller parameters. Such development will enable the various time- and frequency-domain algorithms developed for the harmonic assessment of linear PWM inverters to be applied to hysteresis controlled inverters.

Harmonic load flow studies of systems incorporating inverters with hysteresis current control can be formulated based on the developed models. The iterative solution of the harmonic load flow shall incorporate the harmonic magnitudes and angles obtained from the developed models for a faster convergence to the steady state solution.

## 7. Appendix - A

Function  $f(x) = \frac{\sin(\pi x)}{x(1-x)}$ ,  $x \in [0, 1]$  satisfies  $\lim_{x \rightarrow 0} f(x) = \lim_{x \rightarrow 1} f(x) = \pi$ , is continuous, convex and has even symmetry in  $[0, 1]$ . The approximation of  $f(x)$  in  $[0, 1]$ ,  $\bar{f}(x) = A \cdot \sin(\pi x) + \pi$ ,

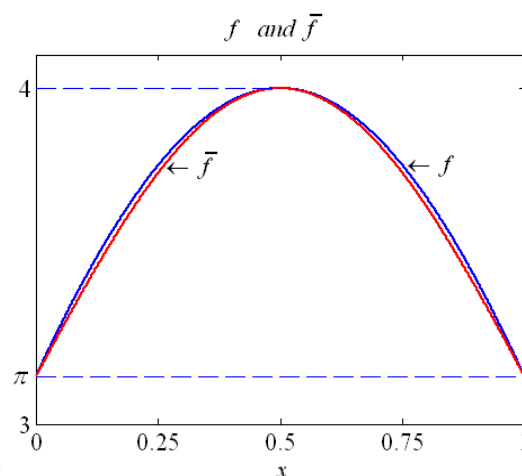


Fig. A1. Approximation of  $f(x) = \frac{\sin(\pi x)}{x(1-x)}$  by  $\bar{f}(x) = (4 - \pi) \cdot \sin(\pi x) + \pi$ .

satisfies the same properties in  $[0, 1]$ . Subsequently, constant  $A$  is calculated such that the square error over the interval  $[0, 1]$   $\Delta f^2 = \int_0^1 (f(x) - \bar{f}(x))^2 dx$  is minimized. Substituting the expressions of  $f(x)$  and  $\bar{f}(x)$  into the mean-squared-error  $\Delta f^2$  and evaluating the integrals numerically yields a function of the parameter  $A$ , as  $\Delta f^2(A) = 0.5A^2 - 0.858A + 0.3833$ . Therefore, the value of  $A$  that minimizes  $\Delta f^2$  is  $A = 0.858$  or  $A = 4 - \pi$ . Functions  $f(x)$  and  $\bar{f}(x)$  are shown in Fig. A1.

## 8. References

- Albanna, A. & Hatziadoniu, C. J. (2009). Harmonic Analysis of Hysteresis Controlled Grid-Connected Inverters, *proceedings of the Power Systems Conference and Exposition*, Seattle, WA, March, 2009.
- Albanna, A. & Hatziadoniu, C. J. (2009). Harmonic Modeling of Single-Phase Three-Level Hysteresis Inverters, *proceedings of the North American Power Symposium*, Starkville, Mississippi, October, 2009
- Albanna, A. & Hatziadoniu, C. J. (2009). Harmonic Modeling of Three-Phase Neutral-Point Inverters, *proceedings of the North American Power Symposium*, Starkville, Mississippi, October, 2009
- Albanna, A. & Hatziadoniu, C. J. (2010). Harmonic Modeling and Analysis of Multiple Residential Photo-Voltaic Generators, *proceedings of the Power and Energy Conference at Illinois*, Urbana-Champaign, Illinois, February 2010
- Albanna, A. & Hatziadoniu, C. J. (2010). Harmonic Modeling of Hysteresis Inverters in Frequency Domain", *IEEE Transactions on Power Electronics*, May 2010



## **Applications of MATLAB in Science and Engineering**

Edited by Prof. Tadeusz Michalowski

ISBN 978-953-307-708-6

Hard cover, 510 pages

**Publisher** InTech

**Published online** 09, September, 2011

**Published in print edition** September, 2011

The book consists of 24 chapters illustrating a wide range of areas where MATLAB tools are applied. These areas include mathematics, physics, chemistry and chemical engineering, mechanical engineering, biological (molecular biology) and medical sciences, communication and control systems, digital signal, image and video processing, system modeling and simulation. Many interesting problems have been included throughout the book, and its contents will be beneficial for students and professionals in wide areas of interest.

### **How to reference**

In order to correctly reference this scholarly work, feel free to copy and paste the following:

Ahmad Albanna (2011). Modeling & Simulation of Hysteresis Current Controlled Inverters Using MATLAB, Applications of MATLAB in Science and Engineering, Prof. Tadeusz Michalowski (Ed.), ISBN: 978-953-307-708-6, InTech, Available from: <http://www.intechopen.com/books/applications-of-matlab-in-science-and-engineering/modeling-simulation-of-hysteresis-current-controlled-inverters-using-matlab>

**INTECH**  
open science | open minds

### **InTech Europe**

University Campus STeP Ri  
Slavka Krautzeka 83/A  
51000 Rijeka, Croatia  
Phone: +385 (51) 770 447  
Fax: +385 (51) 686 166  
[www.intechopen.com](http://www.intechopen.com)

### **InTech China**

Unit 405, Office Block, Hotel Equatorial Shanghai  
No.65, Yan An Road (West), Shanghai, 200040, China  
中国上海市延安西路65号上海国际贵都大饭店办公楼405单元  
Phone: +86-21-62489820  
Fax: +86-21-62489821

© 2011 The Author(s). Licensee IntechOpen. This chapter is distributed under the terms of the [Creative Commons Attribution-NonCommercial-ShareAlike-3.0 License](https://creativecommons.org/licenses/by-nc-sa/3.0/), which permits use, distribution and reproduction for non-commercial purposes, provided the original is properly cited and derivative works building on this content are distributed under the same license.

IntechOpen

IntechOpen